Atomic-Resolution TEM Revealing Structural Complexity of Intermetallic Compounds

Paul Simon[1], Wilder Carrillo-Cabrera, Yuri Grin[2] and Reiner Ramlau

First achievements of the TEM laboratory at MPI CPfS of atomic-resolution imaging comprised host-guest systems of clathrates and skutterudites as well as ultra-hard boron carbide ceramics. Analysis of real structures of superconductors, thermoelectrics and complex catalysts such as Co_4Al_{13} contributed to a better understanding of their chemical as well as their physical properties. Current investigations focus on the exchange interface of left- and right-handed chiral Weyl semimetal CoSi and the atomic-scale analysis of polymorphism in the composition series of the ternary superconducting $Y_{3+x}\{Rh,Ir\}_4Ge_{13-x}$, representing a member of the Remeika family. Chemically different local atomic arrangements were verified in the intermetallic compound $Mg_{29-x}Pt_{4+y}$ comprising more than 400 atoms in the unit cell.

TEM lab history

The TEM lab started in the year 2000, when the first microscope of the institute – a Tecnai F30 by Philipps N. V. – was installed. The microscope was operated at 300 kV and achieved a nominal point resolution of 2.0 Å. In the meantime, structural tasks demanded for higher resolution capabilities. Thus, in the year 2014, a JEM-ARM300F by the manufacturer JEOL was installed, called the Dresden Grand Atomic Resolution Microscope (G-ARM). It was worldwide the first commercial G-ARM and was considered the best TEM at this time. The microscope is equipped with two correctors, one of them for bright field TEM (image) operation and the second for scanning STEM mode (beam), besides an imaging filter for elemental analysis. The improved resolution capabilities were achieved due to corrections of fourth-order axial coma aberration reaching down to 0.66 Å for TEM and 0.40 Å for STEM mode. In combination with targeted focused ion beam sample preparation and scanning electron microscopy (SEM) combined with electron backscattered diffraction (EBSD) techniques regions of specific interest could be selected and prepared for TEM investigations.

First results with the high-end microscope were achieved on clathrates which are structurally complex materials with a large number of atoms in the unit cell. They are composed of covalently bonded framework filled by guest atoms. These compounds are characterized by a low thermal conductivity making them interesting semiconductor materials especially for thermoelectric applications. High-end aberration-corrected STEM images on high-quality single crystals of $Ba_8Ge_{40}Au_6$ showed that Ba2 and Au/Ge1 atoms are displaced from their ideal positions, resulting in deviations from the translational symmetry with randomly distributed Ge and Au atoms [1]. The clathrate $K_7B_7Si_{39}$ was the first borosilicide to be synthesized with boron as framework atoms. It was shown that the presence of boron in the host framework leads to a considerable deformation of the cage cavities, influences the occupancy of the cage with guest atoms and causes displacements of the guest sites from the cage centers [2]. The question about the electron-precise character of boron carbide could be answered and better understanding of the physical properties has been established [3].

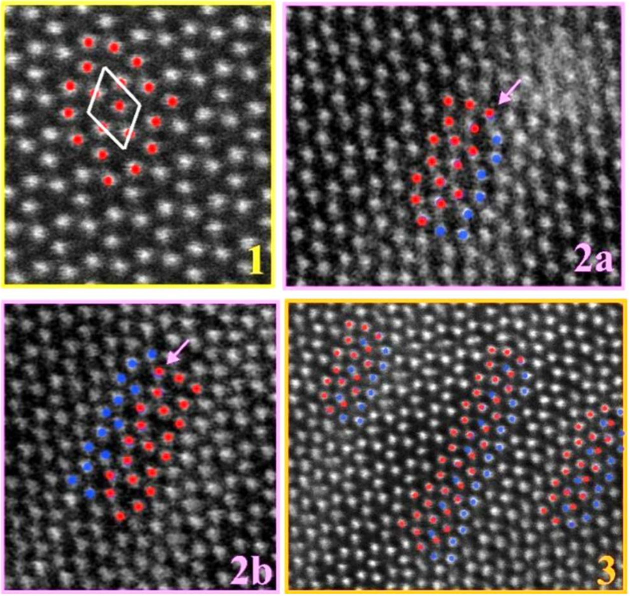

Fig. 1: Local atomic arrangement in the real structure of Be_2Ru [001] by atomic resolution HAADF-STEM; bright dots correspond to the columns of Ru atoms. Six-member rings of Ru atoms in the pristine Fe_2P atomic arrangement with the unit cell highlighted with white lines (1); coherent interface boundaries (pink arrows) between the two types of inversely oriented Ru layers (red and blue) in the plane (2a and 2b); two very close Ru positions can be explained by different atomic arrangements in the neighboring atomic layers along the [001] projection (3).

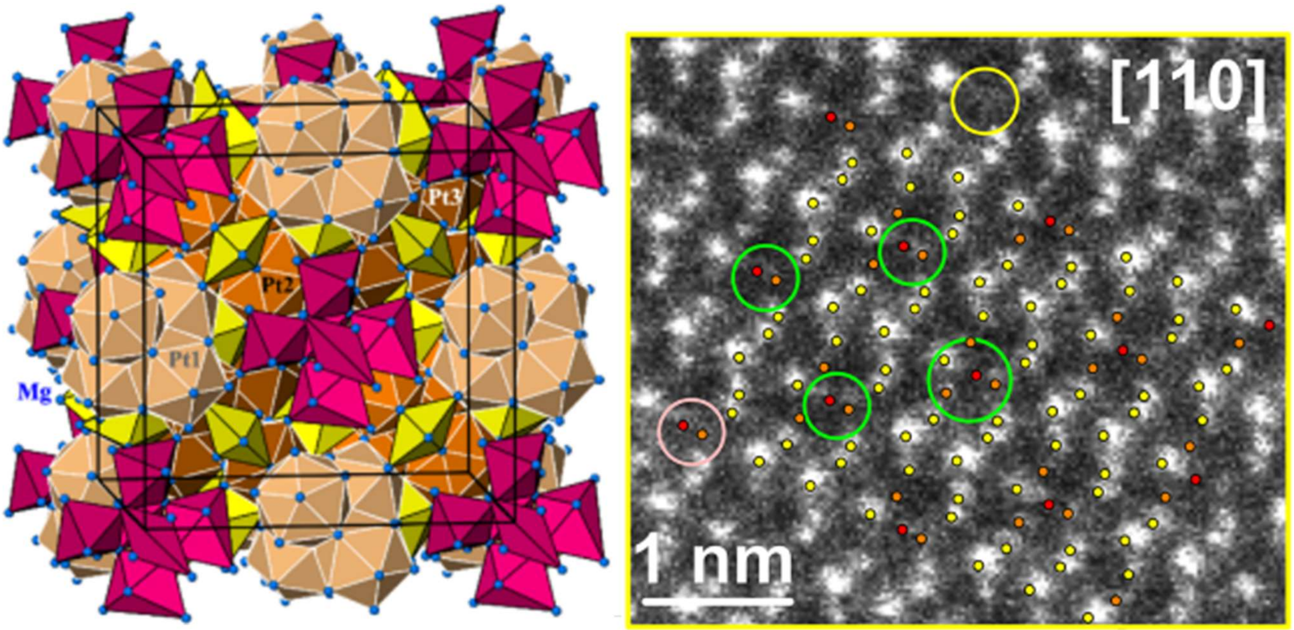

Fig. 2: (Left) Organization of the chemical bonding in $Mg_{29-x}Pt_{4+y}$. (Right) Atomic-resolution HAADF-STEM image of $Mg_{29-x}Pt_{4+y}$ along [110]; only Pt atoms are registered. Positions of Pt atoms: yellow dots -Pt1, Pt2, or Pt3, orange dots -Pt at the Mg11 position, red dots -Pt at the Mg8 position. Different regions with predominant Pt order are marked as yellow, green and pink circles.

The catalyst $Al_{13}Co_4$ possess a huge unit cell with about 102 atoms and is called complex metallic alloy (CMA), which shows features of a quasicrystal approximant. Aberration-corrected high-resolution STEM revealed a much more complex crystal structure besides the regular one, encompassing multiple split and partially occupied crystallographic sites. Even though the whole single crystal shows long-range order, due to the disorder of the aluminum sub-motive every unit cell becomes unique [4]. Lead telluride is a prominent thermoelectric material already in use since the sixties as power supply *e.g.* in the Viking space mission to Mars. The reversible change in its conductive behavior around 270°C from metallic to semi-conductive was uncovered by in-situ temperature-dependent TEM. Stereo-chemically parallel aligned lone pairs of lead below 270°C are responsible in gap closure of the band structure leading to metallic transport behavior [5, 6].

Structural complexity in the apparently simple crystal structure of Be_2Ru

The structural features of the hexagonal layered crystal structure of Be_2Ru were investigated by single crystal X-ray diffraction and transmission electron microscopy supported by analysis of chemical bonding (Figure 1) [7], (see **CMS_02_Leithe-Jasper**). The residual electron density and high-resolution TEM images show that the real structure can be described as an intergrowth of the main hexagonal matrix of the Fe_2P type with minor orthorhombic inclusions of its stacking variants. Such atomic arrangement is stabilized by the charge transfer from Be to Ru and by a system of polar three- and four-atomic bonds involving both components.

Mg_{29-x} Pt_{4+y}: Chemical bonding inhomogeneity and structural complexity

$Mg_{29-x}Pt_{4+y}$ belongs to the family of complex intermetallic compounds crystallizing in the cubic space group $F4\text{-}3m$ with $a = 20.1068(2)$ Å comprising *ca.* 400 atoms. The unit cell represents interpenetrating and face-sharing clusters with different crystallographic types originating from nested polyhedral units located at the high-symmetry points in the unit cell (Figure 2, left). The local disorder around the unit cell origin was imaged with atomic-resolution high-angle dark-field scanning TEM [8], (**CMS_02_Leithe-Jasper**). Four different local atomic arrangements could be verified showing pre-dominantly the positions of Pt atomic columns (Figure 2, right). The regions revealed besides the "regular" Pt atoms Pt1, Pt2, and Pt3 (yellow dots), additional Pt (orange dots) at the positions Mg11 (green circles) and Pt (red dots) at Mg8 (pink circle), as well as regions where Pt was absent at these positions (yellow circle).

Local enantiomorph conversion in single crystals of the Weyl semimetal CoSi

Chiral intermetallic phases show unusual chemical and physical properties with a non-trivial structure-property relationship. It is therefore of particular interest to study the structural conversion between domains of different handedness. Here, the atomic decoration of the enantiomorph exchange area within single crystal of the Weyl semimetal CoSi is determined by a combination of EBSD, atomic resolution STEM imaging (Figure 3), single crystal X-ray diffraction and quantum chemical analysis of atomic interactions [9], (see **CMS_06_Burkhardt**).

Two-atomic [CoSi] units may be considered as ‘pseudo-molecules’, thinking of molecular organic crystals. A tiny reorganization of atomic interactions within these units results in the appearance of sequence ‘faults’ in the structure pattern i.e. in a different structural motif in the enantiomorph exchange area, which – contrary to the A and B enantiomorphs of CoSi – contains an inversion center and allows a local enantiomorph ‘conversion’. Due to the special features of atomic interactions, the reorganization of multi-atomic bonds leads to slightly higher total energy. This appears within one and the same grain. Atomic-resolution STEM HAADF images in three crystallographic directions show the periodicity of 4.45 Å along [010], being parallel to the enantiomorph exchange region (Figure 3). The images on the left and the right sides of each panel can be easily understood as the pristine matrix of the CoSi B and A forms, respectively (light blue- and red-marked unit cells), as established by EBSD on the microscale level. If the image is overlaid with the projection of the crystal structures of both enantiomorphs, one recognizes that in the middle region the A and B lattices do not match (bottom part of each panel in Figure 3). A shift of $\Delta \approx 0.2a$ CoSi parallel to [100] appears between the lattices of the A- and B-form. The arrangement of the atomic columns in this region is not found in the regular A- or B-form regions.

From the bonding point of view, the basic building block of the structure is the polar two-atomic Co-Si unit. Projected along [100], such units form the characteristic zigzag patterns in both enantiomorph forms of CoSi (Figure 4, top), which are also recognizable in the HR-STEM HAADF images, if the spots with different intensity are connected pairwise (Figure 3). The two-atomic Co-Si units are also present in the models of the enantiomorph exchange area. While in the peripheral regions their zigzag-like arrangement agrees with that in the A and B forms of CoSi, a kind of sequence ‘fault’ appears in the middle region (Figure 4, bottom).

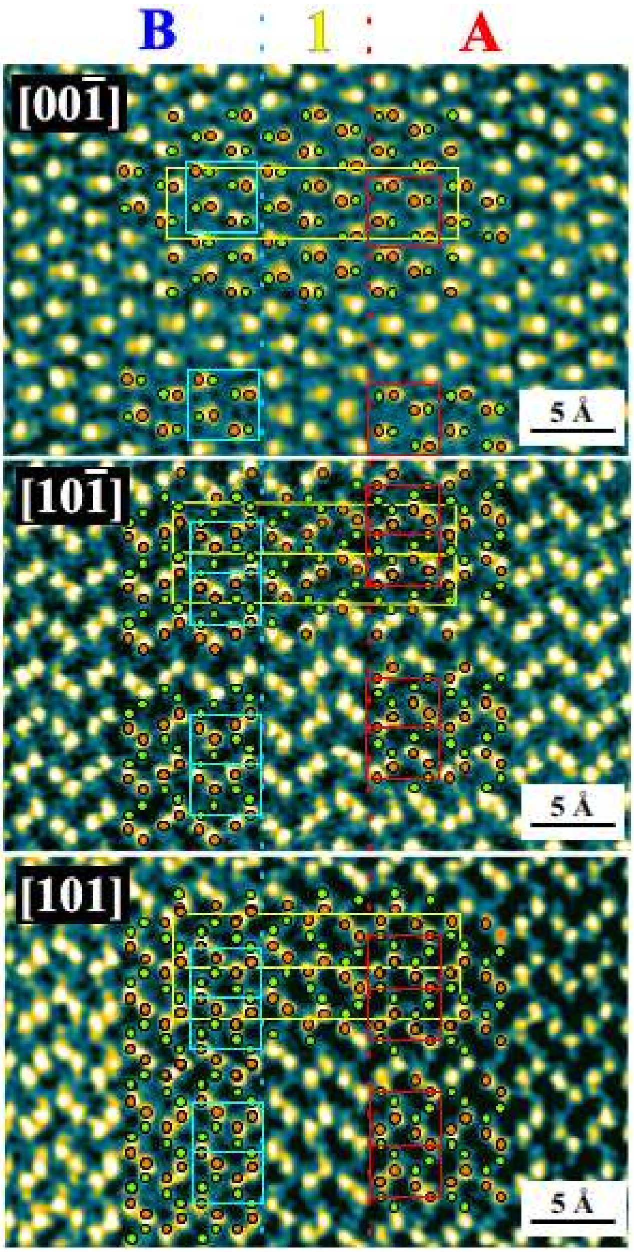

Fig. 3: CoSi enantiomorph exchange area. Aberration-corrected high angular dark field STEM images of the enantiomorph exchange area (yellow 1) in the CoSi along the direction (a) [00-1], (b) [10-1], (c) [101]. The images are superimposed with the structure models of CoSi form B (unit cell - light blue), CoSi form A (unit cell – red) and P21/c model (unit cell - yellow, Co - orange, Si - green).

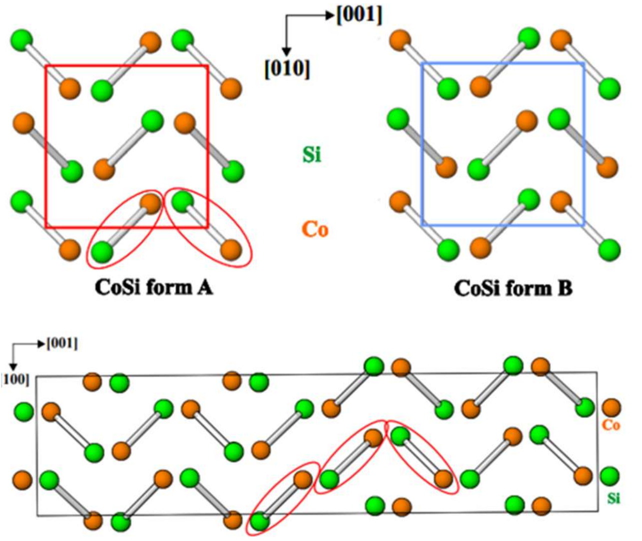

Fig. 4: (top) Schematic representations of the A and B forms of CoSi by basic bonding blocks – Co-Si pairs. (bottom) Chemical bonding within the enantiomorph exchange area in CoSi. Schematic representation of the monoclinic structure by basic bonding blocks – Co-Si pairs. The enantiomorph exchange region with the sequence 'fault' emphasized by red marks.

Composition-dependent polymorphism of the superconductor $Y_{3+x}\{Rh,Ir\}_4Ge_{13-x}$

Polymorphism is observed in the $Y_{3+x}Rh_4Ge_{13-x}$ series of compounds. The decrease of Y-content leads to the transformation of the primitive cubic $Y_{3.6}Rh_4Ge_{12.4}$ [$x = 0.6$, space group *Pm*-3*n*], adopting a strongly disordered structure of the $Yb_3Rh_4Sn_{13}$ prototype, into a body-centered cubic structure [$x = 0.4$, $I4_132$,] and further into a tetragonal arrangement [$x = 0$, $I4_1/amd$] for stoichiometric $Y_3Rh_4Ge_{13}$. Compounds from the $Y_{3+x}Rh_4Ge_{13-x}$ series are found to be weakly-coupled BCS-like superconductors with T_c = 1.25 K, 0.43 K and 0.6 K, for x = 0.6, 0.4 and 0, respectively, showing low thermal conductivity and small Seebeck coefficients. The latter are common for metallic systems. $Y_3Rh_4Ge_{13}$ undergoes a first-order phase transition at T_f = 177 K, with signatures compatible to a charge density wave scenario. The [100] HR-TEM images obtained for the $Y_{3+x}Rh_4Ge_{13-x}$ series are illustrated in Figure 5. Projections of the structure models obtained from the PXRD structure refinements are inserted in the respective HR-TEM images [10].

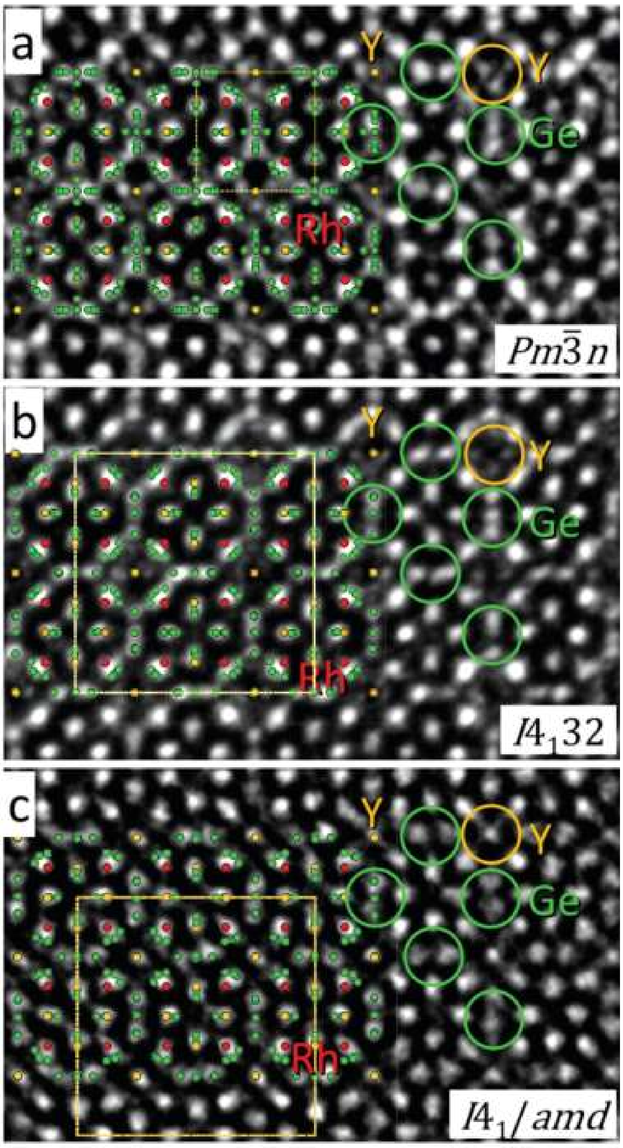

Fig. 5: HR-TEM images along [100] direction for (a) $Y_{3.6}Rh_4Ge_{12.4}$ *(Pm-3n type domain), (b)* $Y_{3.4}Rh_4Ge_{12.6}$ *(*$I4_132$ *type area) and (c)* $Y_3Rh_4Ge_{13}$ *(*$I4_1/amd$ *type). Projections of the corresponding structure models are inserted in the images. Three germanium columns (green circles) and one Y column (yellow circle) are marked to emphasize the local differences*

External Cooperation Partners

Roman Gumeniuk (Universität Freiberg); Umut Aydemir and Havva Funda Yağcı Acar (Koç University Istanbul Turkey); Hermann Ehrlich, (University of Poznan)

References

[1] *Direct measurement of individual phonon lifetimes in the clathrate compound* $Ba_{7.81}Ge_{40.67}Au_{5.33}$. *P.-F Lory, S. Pailhès, V.M. Giordano, H. Euchner, H.D. Nguyen, R. Ramlau, H. Borrmann, M. Schmidt, M. Baitinger, M. Ikeda, P. Tomes, M. Mihalkovic, C. Allio, M.R. Johnson, H. Schober, Y. Sidis, F. Bourdarot, L.P. Regnauls, J. Ollivier, S. Paschen, Y. Grin and M. de Boissieu, Nat. Comm.* **8** *(2017) 491,* https://doi.org/10.1038/s41467-017-00584-7

[2] $K_7B_7Si_{39}$, *a borosilicide with the clathrate I structure, W. Jung. J. Lörincz, R. Ramlau, H. Borrmann, Y.Prots, F. Haarmann, W. Schnelle, U.Burkhardt, M. Baitinger, Y. Grin, Ang. Chem. Int. Ed.* **46** *(2007) 6725–6728,* https://doi.org/10.1002/anie.200701028

[3] *Local atomic arrangements and band structure of boron carbide, K. Rasim, R. Ramlau, A. Leithe-Jasper, T. Mori, U. Burkhardt, H. Borrmann, W. Schnelle, C. Carbogno, M. Scheffler and Y. Grin, Angew. Chem. Int. Ed.* **57** *(2018) 6130,* https://doi.org/10.1002/anie.201800804

[4] *Structural complexity of the intermetallic compound* $o\text{-}Al_{13}Co_4$. *P. Simon, I. Zelenina, R. Ramlau, W. Carrillo-Cabrera, U. Burkhardt, P. Gille, Y. Grin, J. Alloy Compd.* **804** *(2020) 153363,* http://dx.doi.org/10.1016/j.jallcom.2019.153363

[5] *Structural complexity of PbTe single crystals. I. Zelenina, P. Simon, I. Veremchuk, X. Wang, M. Bobnar, W. Lu, C.H. Liebscher, Y. Grin. Commun. Mater.* **2** *(2021) 99,* https://doi.org/10.1038/s43246-021-00201-7

[6] *In-situ observation of electron-beam-induced formation of nano-structures in PbTe, I. Zelenina, I. Veremchuk, Y. Grin, P. Simon. Nanomaterials* **11** *(2021) 163,* https://doi.org/10.3390/nano11010163

[7]* *Structural complexity in the apparently simple crystal structure of* Be_2Ru, *L. Agnarelli, Y. Prots, A. Ormeci, R. Ramlau, M. Krnel. E. Svanidze, M. König, M. Schmidt, U. Burkhardt, A. Leithe-Jasper, Y. Grin, Chem. Eur. J.* **29** *(2023) e202300578,* https://doi.org/10.1002/chem.202300578

[8]* $Mg_{29-x}Pt_{4+y}$.: *Chemical bonding inhomogeneity and structural complexity, L. Agnarelli, Y. Prots, R. Ramlau, M. Schmidt, U. Burkhardt, A. Leithe-Jasper, Y. Grin, Inorg. Chem.* **61** *(2022) 16148–16155,* https://doi.org/10.1021/acs.inorgchem.2c02653

[9]* *Enantiomorph 'conversion' in the single crystals of Weyl semimetal CoSi, W. Carrillo-Cabrera, P. Simon, M. Schmidt, M. König, H. Borrmann, A. Winkelmann, U. Burkhardt, Y. Grin, Commun. Mater.* **4** *(2023) 109,* https://doi.org/10.1038/s43246-023-00434-8

[10]* *Composition dependent polymorphism and super-conductivity in* $Y_{3+x}\{Rh,Ir\}_4Ge_{13-x}$, *M. Feig, W. Carrillo-Cabrera, M. Bobnar, P. Simon, C. Curfs, V. Levytskyi, A.A. Tsirlin, A. Leithe-Jasper, R. Gumeniuk, Dalton Trans.* **51** *(2022) 4734–4748,* https://doi.org/10.1039/D2DT00167E

---

[1] simon@cpfs.mpg.de

[2] grin@cpfs.mpg.de